Article

Not peer-reviewed version

Numerical analysis of the TRC shells: Basic principles

Iurii Vakaliuk *, Silke Scheerer, Manfred Curbach

Posted Date: 11 December 2023

doi: 10.20944/preprints202312.0705.v1

Keywords: Textile reinforced concrete; TRC; shell; material characteristics; material model; numerical investigation

Preprints (www.preprints.org) | NOT PEER-REVIEWED | Posted: 11 December 2023 doi:10.20944/preprints202312.0705.v1

Article

Numerical Analysis of the TRC Shells: Basic Principles

Iurii Vakaliuk *, Silke Scheerer and Manfred Curbach

Institute of Concrete Structures, TUD Dresden University of Technology (Germany);
silke.scheerer@tu-dresden.de (S.S); manfred.curbach@tu-dresden.de (M.C.)
* Correspondence: iurii.vakaliuk@tu-dresden.de; Tel.: +49-351-463-36110

Abstract: In the case of solid slabs made of reinforced concrete that are usually subjected to bending, large areas of the structure are stressed well below their load-bearing capacity or remain stress-free. Contrary to this are shell structures, which can bridge large spans with little material if designed well. To improve the efficiency of ceiling slabs, we want to utilize the shell load-bearing behaviour on a smaller scale by dissolving the solid interior accordingly. In order to be able to study a wide range of such constructions virtually, a parametric multiobjective simulation environment is to be developed in an ongoing research project, basic analysis approaches of which are presented in this paper. In addition to the basic workflow and the programs used, the material models used, and their calibration are described on the basis of tests on textile reinforced concrete (TRC) samples. Initial tests on two individual TRC served to verify the model.

Keywords: textile reinforced concrete; TRC; shell; material characteristics; material model; numerical investigation

1. Introduction

Ceiling slabs made of reinforced concrete usually have a constant, solid cross-section. Under pure bending stress, which is the usual case, many sections of the structure are loaded clearly below their load-bearing capacity or remain free of stress. Overall, the material utilization is not sufficient, and the dead weight is high. This is fundamentally contrary to the absolute requirement of our time to use resources of all kinds as efficiently as possible.

Various methods are known to increase the efficiency of concrete components subjected to bending, which is often based on the principle 'form follow force' or the intelligent combination of materials with different densities and mechanical properties. Examples are [1–3] (adaptation of the outer geometry of a component), [4,5] (sandwich-like layering of different concretes), or [6–8] (inner hollow spaces, generated by hollow bodies, or grading for weight minimization).

In sub-project C01 of the CRC/Transregio 280 "Design Strategies for Material-Minimized Carbon Reinforced Concrete Structures — Principles of a New Approach to Construction" [9,10], a new approach is being explored. We intend to use the outstanding load-bearing behaviour of shell constructions on a smaller scale using textile reinforced concrete (TRC). If the shell shape is adjusted so that the resultant of the decisive continuously acting loads remains in the core cross-section, normal forces predominate. The material is utilized homogeneously (a membrane stress condition). The three-dimensional shape provides stability. The project aims to exploit this load-bearing principle of shells at the component level. The idea is to dissolve the usually solid interior of, e.g., a plate subject to bending into load-bearing shell structures [11]. Thus, the material is used more efficiently, and weight is saved at the same time, without any loss of load-bearing capacity. The paper discusses the basic principles that form the analysis routines to aim reaching this goal.

2. Workflow Overview

One of the most important aspects of the development of a method to deal with curved filigree TRC structures within the scope of the project is the computational workflow that determines how to calculate such structures. The process was developed in the form of three steps. Figure 1 gives a general overview of the steps and their constituent subroutines.

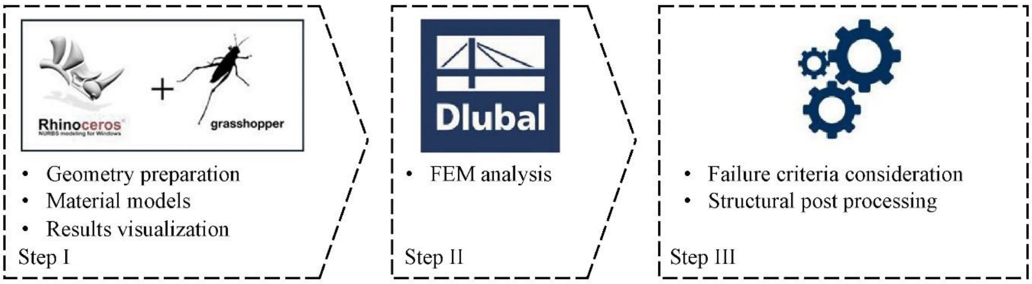

Figure 1. Overview of the workflow, Graphic: Iurii Vakaliuk.

In the first step, the basic geometrical principles of the TRC shell structure are described using the parametric environment of Rhino 3D [12] + Grasshopper 3D [13] (Rh+GH) software packages. Furthermore, Rh+GH processes the other model metadata such as material properties, load cases, boundary conditions, etc. The second step starts when all the required information about the structural model is transferred to the FEM software via the COM interface [14]. Considering two recently successfully finished projects [15,16], the software RFEM [17] from Dlubal Software, Inc. was selected for the current research project. The usage of RFEM as a main FEM solver provides competitively fast processing and stability. The raw data processing from the FEM calculator occurs in Step III. The standalone programs analyze the failure criterion and the utilization ratio and prepare a visualization of the FEM results as well as required statistics. If the failure load is not reached, the process may be performed iteratively between Step II and Step III until the failure of the structure is recognized by the failure criteria programmed modules.

It is important to specify that one part of the components of the calculation routines were directly developed within the Rh+GH environment and another part was implemented in the form of external solutions based on Python or C# scripting language. Such an approach helps to improve the processing speed of the components and make them more independent from each other which in turn adds modularity features to the whole system. The modularity of the workflow supports the integration of more sophisticated analysis methods and failure criteria for TRC structures such as described in [18].

3. Materials Models

3.1 Short Overview of Material Models for TRC

One of the most important points is the way the calculation routines integrate the theoretical background of the TRC structures. In the present state of the art in the field of analysis of TRC structures, three categories of numerical approaches can be summarized [19] which are given in Figure 2 as a schematic overview. The first column (a) shows parameters of the discrete crack model description. Here, the damage to the concrete is considered via the evolution of discrete cracks in the matrix and a nonlinear bond stress-slip relation between concrete and continuous fibre-based reinforcement [19]. The model gives a valuable representation of the composite behaviour but with a considerable level of complexity in the description of the governing mechanisms as well as computational efforts. For the planned iterative workflow, a high numerical complexity implies a disproportionate numerical effort, that is why this approach was not pursued further for the project. In the smeared model (b), TRC is represented as a composite with uniform behaviour over the cross-section. The model's parameters are determined via rule of mixtures that demands correct estimation of volume fractions of the constituents. With that, the material model has to be calculated for each cross-sectional configuration [19]. It should be noted here that the smeared model was the most convenient one within the selected software packages to account for the damage effects in the TRC.

A more detailed description of the model used in RFEM is given later. The third model (c) contains resolved realization of the matrix and textile layers. The behaviour is similar to the discrete model with the difference that the cracks in the matrix are smeared along the specimen. This makes the model less demanding for the numerous calibration procedures and gives opportunity to consider the exact position of the reinforcement layers within the cross-section [19].

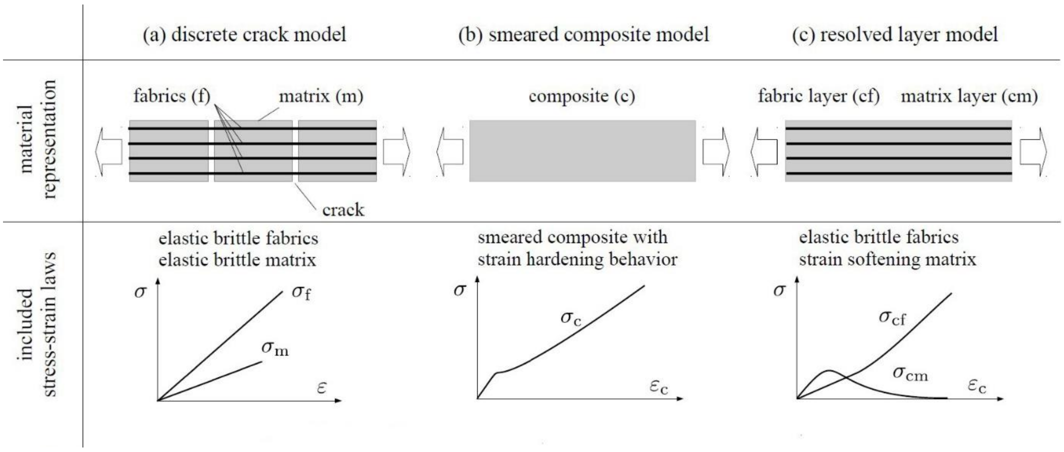

Figure 2. Classification of modelling approaches of textile reinforced concrete under tension including the stress-strain relations in the cross-section, Graphic: Rostislav Chudoba, see [19].

For the calculation in RFEM, a material description for the composite textile reinforced concrete under compressive and tensile stress is required which can be represented by the smeared approach. The stress-strain behaviour of TRC under tension is very similar to that of steel-reinforced concrete, see e.g. [20,21]. In *State I*, the concrete is non-cracked, and the specimen's stiffness is high. The composite's strain ε_c is equal to the strains in matrix ε_m and the fibre reinforcement ε_f. When the concrete's tensile strength is reached, cracks begin to form successively (*State IIa*). If the tensile force is increased further beyond the point of completed cracking, the number of cracks no longer changes. Only the crack widths increase (*State IIb*) until the textile tears. As part of the described workflow (Figure 1), a special script was developed within the scope of Rh+GH environment, with which multiple experimental results of a test series were converted into a single average curve of the stress-strain relation. Afterwards the script converts this average data curve into three states I to IIb to be able to map the curve analytically for further processing.

The analytical description should reflect the material behaviour of TRC as accurately as possible. This is important for the further optimization and analysis of the textile reinforced concrete shell structures in the context of a theoretical parametrical study, as only singular structures can be tested in the experiment. However, we would like to be able to make a statement about the behaviour of structures with different geometries, material combinations and loading scenarios. There are several analytical models appropriate for TRC, each with specific advantages and disadvantages. The following two were shortlisted:

- ACK model is named after its creators Aveston, Cooper and Kelly, and was published in 1971. The key aspect of the model is that it is one of the most numerically simple and is based on simplified assumptions describing the effect that happens inside the TRC sample under the tensile action [20].
- Trilinear model is based on the approach of three linear, continuously ascending ranges which are adapted from the real stress-strain line of TRC. The slope and other parameters can be determined according to the rule of mixtures, appropriate efficiency factors and recommendations from Model Code 90 [22–24].

The common approach, valid for each of the material model is that the experimental data can be approximated by idealized first-order polynomials, see e.g. [20]:

$$\boldsymbol{y_i} = m \cdot \boldsymbol{x_i} + n \tag{1}$$

with the coefficients m and n which determine the slope and the intercept of the polynomial respectively; $\boldsymbol{y_i}$ and $\boldsymbol{x_i}$ are experimental data points.

3.2 ACK material Model

ACK model possesses one key feature: a simple analytical assembly. The simplicity is governed by accepted assumptions such as the perfect bond between matrix and fibers, behaviour according to the theory of elasticity, the law of mixtures and the assumption of essentially constant stress level in the crack formation phase (State IIa) [20]. Figure 3 shows the principal behaviour with all the respective components.

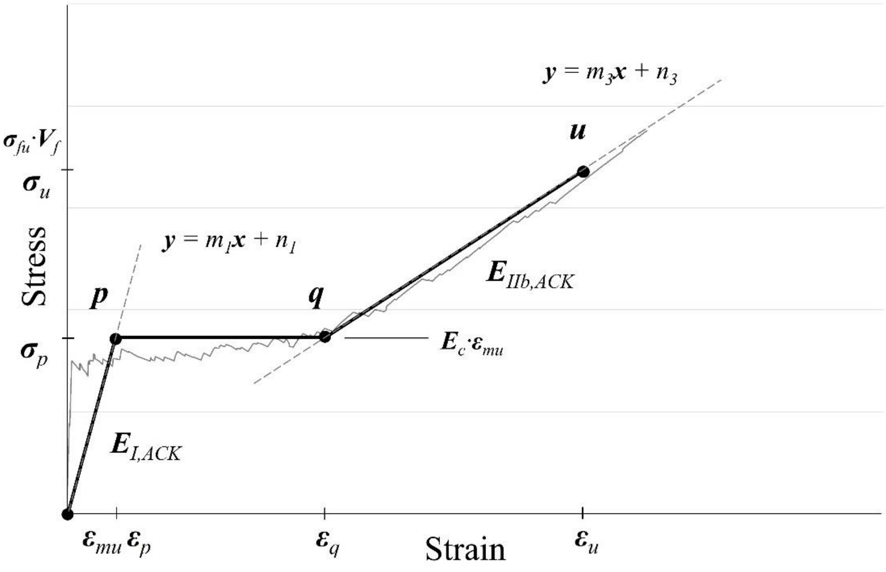

Figure 3. Principle of the ACK material model, Graphic: Iurii Vakaliuk.

Based on experimental data, the coefficients of the first-order polynomial equations can be calculated in general form using linear regression principles with the least squares method. The experimental data and least square method give E modulus values for the TRC material only for State I and State IIb according to the assumptions made before. The respective values can be expressed as follows [20,22,25,26]:

$$E_{I,ACK} = E_f \cdot V_f + E_m \cdot \left(1 - V_f\right) \tag{2}$$

$$E_{IIb,ACK} = E_f \cdot V_f \cdot \eta_{IIb,ACK} \tag{3}$$

where $E_{I,ACK}$ (MPa) and $E_{IIb,ACK}$ (MPa) are the composite's stiffnesses of a TRC sample in State I and State IIb respectively; V_f symbolizes the fibre volume fraction calculated as $V_f = A_{tex}/A_c$, with A_{tex} the cumulative area of the textile reinforcement and A_c the total sample cross-section in (mm^2); $\eta_{IIb,ACK}$ is an efficiency factor of the textile reinforcement. Reduction of the reinforcement efficiency can be explained with influence of failure of the sleeve fibers and bundle effect [27]. For a proper determination of the multilinear law, the transition points have to be located as follows:

$$\varepsilon_p = \frac{\sigma_{mu}}{E_m} \tag{4}$$

$$\varepsilon_q = \frac{\sigma_{mu}}{E_f \cdot V_f \cdot \eta_{IIb,ACK}} - C \cdot \alpha_e \cdot \sigma_{mu} \tag{5}$$

where σ_{mu} (MPa) is the matrix tensile strength at failure (first crack); ε_p and ε_q are strain levels for points p and q acc. to Figure 3. The numerical constant C depends on the crack spacing and has to be

doi:10.20944/preprints202312.0705.v1

calibrated. The given calculation concept can be used to derive stress-strain relation of composites with various fibre types [22]. Homogenization coefficient α_e can be calculated via Eq. (6):

$$\alpha_e = \frac{E_m \cdot (1 - V_f)}{E_f \cdot V_f \cdot \eta_{IIb,ACK}} \tag{6}$$

The ultimate point u defines the tensile limit of the composite material. The associated material values are:

$$\sigma_u = \sigma_{u,tex} \cdot V_f \cdot \eta_{IIb,ACK} \tag{7}$$

$$\varepsilon_u = \varepsilon_q + \frac{\sigma_u - \sigma_q}{E_f \cdot \eta_{IIb,ACK}} \tag{8}$$

where $\sigma_{u,tex}$ is the tensile limit of the textile reinforcement in (MPa).

3.3 Trilinear Material Model

An alternative concept for modelling the tensile behaviour of TRC composite is a solution introduced by Nathan et al. [23] in 1977 using a trilinear stress-strain curve characterized by three linear ranges similar to that of the ACK model [22]. However, the line in the 2nd area is not horizontal but slightly ascending (Figure 4). The slope of the line in each range is calculated in similar way using a rule of mixtures, combined with the appropriate efficiency factors. The determination of the factors is the objective for further material model calibration.

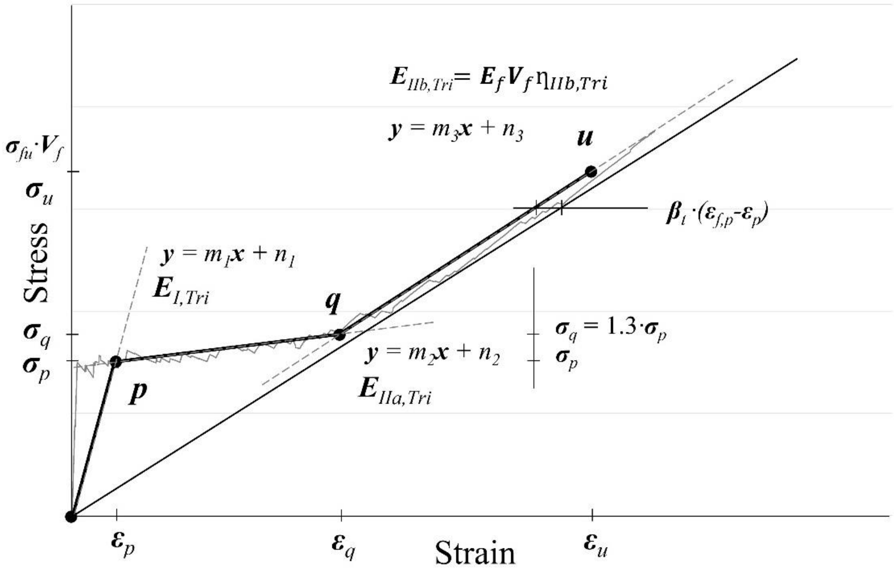

Figure 4. Principle of the trilinear material model, Graphic: Iurii Vakaliuk.

The trilinear material model gives a similar representation for the uncracked zone like the ACK model. The reason for that similarity lies in the basic principles that describe the material according to the rule of mixtures and the joint assumption that until the initiation of a first crack in the composite, the compatibility of strain between the fibre and the matrix is satisfied [23]. Thus, the strain level ε_p for point p can be similarly calculated via the Eq. (10) with respective level of the matrix tensile strength σ_{mu} and elastic modulus $E_{I,Tri}$ (MPa) for the uncracked range State I. In the further description, the rules based on MODEL CODE 90 guidelines of tension-stiffening effects acc. to [5,24]. The next point q with σ_q and ε_q can be calculated using Eqn. (9), (10) [28]:

$$\sigma_q = 1.3 \cdot \sigma_p \tag{9}$$

$$\varepsilon_q = \varepsilon_{f,q} - \Delta\varepsilon \tag{10}$$

where $\varepsilon_{f,q}$ is the strain of the reinforcement in a crack. For the calculation of the composite's strain in point q, at first, the strain of the pure reinforcement is calculated for the loading at this load level σ_q. The associated strains differ between embedded reinforcement and pure resp. unembedded grid. The difference $\Delta\varepsilon$ reflects the influence of the tension stiffening effect and may be considered via:

$$\Delta\varepsilon = \beta_t \cdot \left(\varepsilon_{f,p} - \varepsilon_p\right) \tag{11}$$

where β_t is the integration factor for the reinforcement strain along the transmission length; $\varepsilon_{f,p}$ the fibre strain at the point of zero slip under first crack forces reaching σ_{mu}; ε_p the fibre strain in the crack under cracking stress reaching $f_{\mathrm{ctm}}(t)$ [24]. A factor of 1.3 is recommended as the difference between σ_p and σ_q for TRC samples acc. to [20]. In addition, the composite's stiffness E_{IIa} in the area of successive crack formation after the first crack can be described using principle of first-order polynomial approximation as follows:

$$E_{IIa,Tri} = k \cdot E_m \cdot V_m + E_f \cdot V_f \tag{12}$$

where $k < 1$ is an empirical parameter accounting for the reduction in the effectiveness of the concrete matrix [29]. The value of k is dependent on the volume fraction of fibres V_f and can be determined e.g., experimentally. The value σ_p thus may be alternatively determined via the intersection of the two first-order polynomial functions that describe State IIa with the slope of $E_{IIa,Tri}$ and State IIb with the slope of $E_{IIb,Tri}$, respectively. There are two close approaches: one based on MODEL CODE 90, Eq. (9), and the other based on geometrical interpretation of Eq. (12). Furthermore, the strain in the State IIa range can be estimated in practical way with Eq. (13):

$$\varepsilon = \varepsilon_{f,p} - \frac{\beta_t \cdot \left(\sigma - \sigma_p\right) + \left(\sigma_q - \sigma\right)}{\sigma_q - \sigma_p} \cdot \left(\varepsilon_{f,p} - \varepsilon_p\right) \tag{13}$$

with $\sigma_p < \sigma \leq \sigma_q$ and $\varepsilon_p < \varepsilon \leq \varepsilon_q$. Hence, the slope of the polynomial of the composite $E_{\mathrm{IIb,Tri}}$ corresponds to a parallel shift of the polynomial of the unembedded reinforcement that is described according to the rule of mixtures similarly to the ACK model as follows:

$$E_{IIb,Tri} = E_f \cdot V_f \cdot \eta_{IIb,Tri} \tag{14}$$

with the experimental factor $\eta_{III,Tri}$ that considers the reduction of the stiffness similarly due to the textile reinforcement bundle effect [27]. The ultimate tensile point u and the respective values of the ultimate stress σ_u and strain ε_u should be determined similarly according to the Eqn. (7) and (8), respectively.

3.4 Calibrating the Selected Material Models

To calibrate the material models and respective parameters it was required to perform uniaxial tensile tests on composite samples. The concrete mixture C3-B2-HF-2-190-2 [30], optimized for fibre reinforcement, was used. With a maximum grain size of 2 mm, it is also suitable for the production of very filigree concrete components. Table 1 provides the mixture [30]. The binder BMK-D5-1 is outside the current cement standard due to the addition of an inert filler and was developed in cooperation between the Institute for Building Materials of TU Dresden and the Deuna cement plant (Dyckerhoff® company) in the project C3-B2 as part of the C³ – Carbon Concrete Composite project [31].

Table 1. Mixture composition of concrete C3-B2-HF-2-190-2 [30].

Raw materials	Quantity (kg/m³)
Binder compound BMK-DS-1 (Dyckerhoff, Germany)	815
Quartz sand 0.06/0.2	340
Sand 0/2	965

Superplasticizer (e.g. MC-VP-16-0205-02 from MC-Bauchemie, Germany)	17
Water	190

The compressive and bending tensile strength of the hardened concrete from Table 2 were determined on 3 prisms with dimensions of 40 × 40 × 160 mm according to DIN EN 196-1 [32].

Table 2. Properties of hardened concrete (mean values)

Property	Value	Unit
Compressive strength f_{cm}	114.8	MPa
Bending tensile strength $f_{ctm,fl}$	8.8	MPa

As carbon fibre textile reinforcement, the solidian GRID Q85-CCE-21-E5 [33] was selected. The factory-guaranteed properties are provided in Table 3 [33].

Table 3. Properties of textile reinforcement solidian GRID Q85-CCE-21 [33]

Property	Longitudinal	Transversal
Roving axis distance e_{tex} (mm)	21	21
Cross-section of a roving A_f (mm$^{2)}$	1.81	1.81
Cross-section of the reinforcement grid A_{tex} (mm^2/m)	85,4	85,6
Tensile strength of the roving $\sigma_{u,f}$ (MPa)	≥ 3,950	≥ 4,250
Tensile strength of the grid $\sigma_{u,tex}$ (MPa)	≥ 3,950 (avg.) ǀ ≥ 3,050 (char.)	≥ 4,250 (avg.) ǀ ≥ 3,250 (char.)
Resisting force F_{tex} (kN/m)	≥ 260,5	≥ 275,0
Modulus of elasticity E_{tex} (MPa)	≥ 251,500	≥ 254,000

For tensile tests on TRC, a 1,220 × 540 × 40 mm slab was concreted and stored the first days under wet cloths and afterwards at 20 °C in a climate chamber with 65 % relative humidity. The plate thickness and the two-layer carbon reinforcement were selected acc. to later planned shell elements. The reinforcement was located centrally with a gap of 10 mm, the concrete covers were equal to 15 mm on both sides of the test samples. Before testing at an age of 28 days, in total six 800 × 62 × 40 mm big tensile test samples were cut off from the slab. The samples were loaded displacement controlled with a loading speed of 0.03 mm/min until failure. In addition to the force, the deformation was recorded with two LVDTs in the measuring range. The test setup presented in Figure 5.

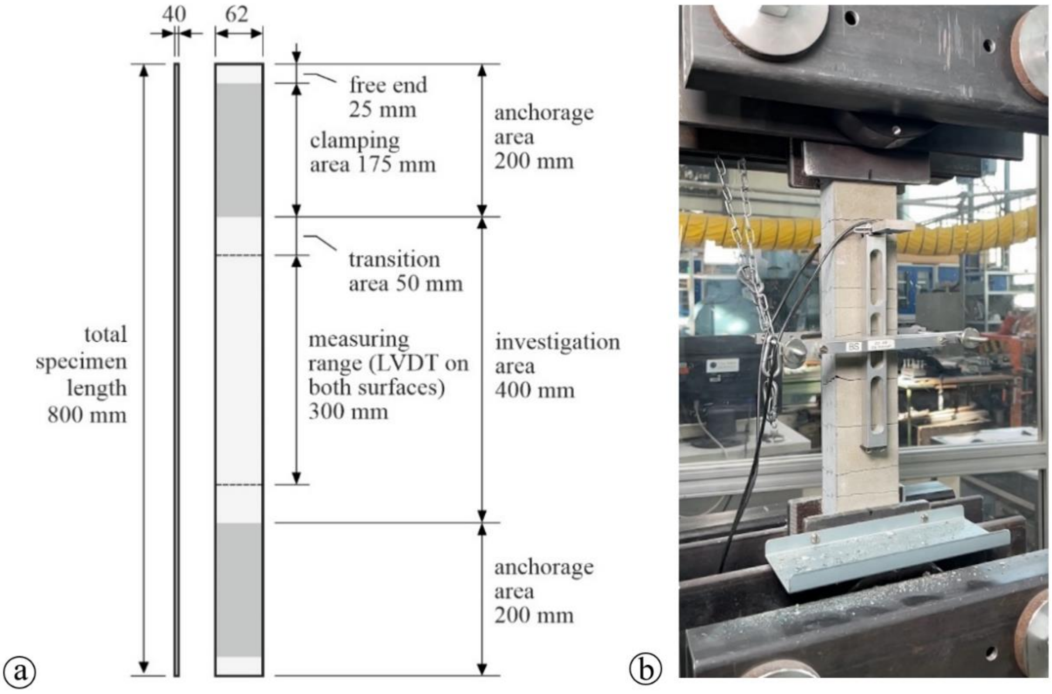

Figure 5. Tensile tests on TRC; (a) sample geometry, (b) sample during testing, Graphic: Silke Scheerer, photo: Iurii Vakaliuk.

The average stress-strain curve from the six individual tests is compared with the material models in the following, the detailed results are published in [34]. Based on the material properties presented, the material models described above were calibrated. Figure 6 shows the results for the ACK material model (M1). Figure 7 displays simulated results for the trilinear model (M2) similarly. For the comparison with the experiments, both models were calibrated with $V_f = 0.40$ %.

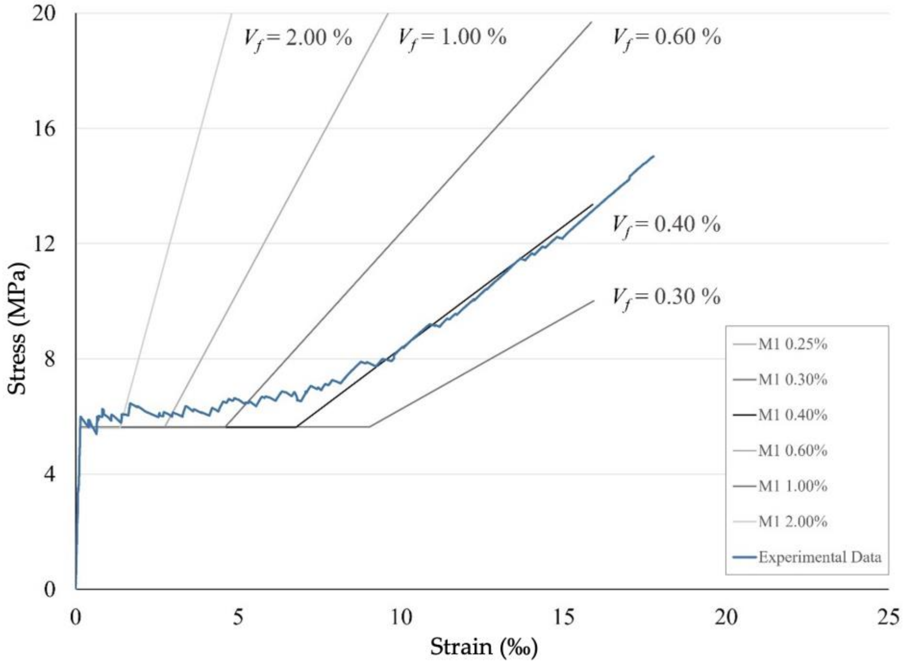

Figure 6. Calibrated ACK material model for various values of volume fraction V_f, Graphic: Iurii Vakaliuk.

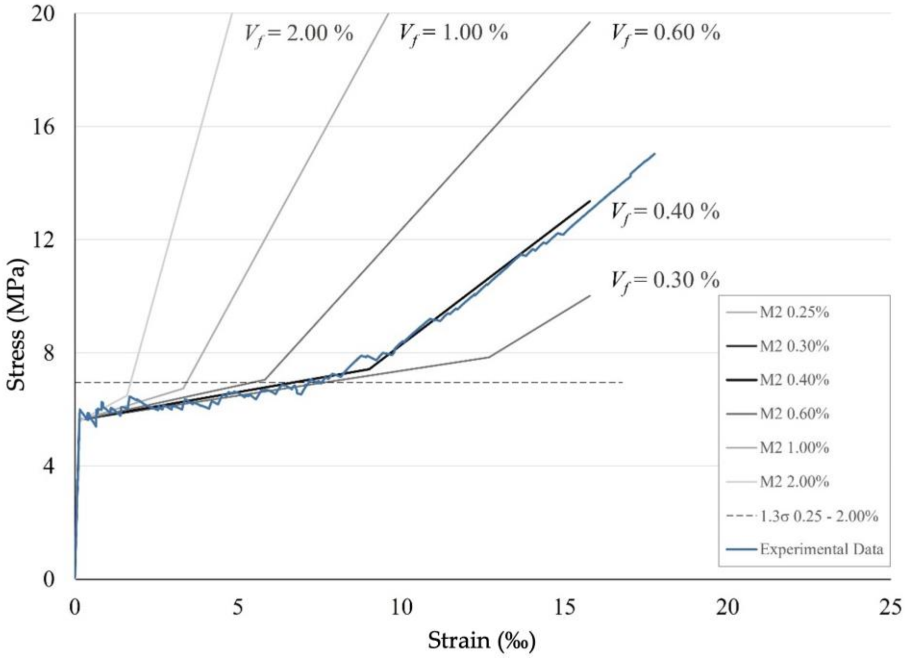

Figure 7. Calibrated trilinear material model for various values of volume fraction V_f, Graphic: Iurii Vakaliuk.

The key characteristic values of the calibrated material models are compiled in Table 4. As expected, the most significant difference between the two models can be seen in State IIa. The M2 model can clearly represent the real material behaviour in this area better than the M1 model, but the key role plays the behaviour of the material models within the scope of numerical analysis, see Chapter 6.

Table 4. Calibrated parameters of the material models

Properties	ACK	Trilinear
E_I (MPa)	42100.0	42100.0
E_{IIa} (MPa)	0.0	201.14
E_{IIb}(MPa)	846.9	843.28
η_{IIb}	0.91	0.91
C	–0.02	–
β_t	–	–0.04
k	–	0.0025

Though the analytical material models significantly simplify the calculation routine, in some features they show some differences to the experimental results. Thus, for instance, for the point p that depict the transition from State I to State IIa, the stress level σ_{mu} equal to the tensile strength of the concrete matrix f_{ctm}. It can be calculated using results derived for the prism tests given in Table 2 according to Eq. (15), [24,28]:

$$f_{ctm,prism} = f_{ctm,fl} \cdot \frac{1.5 \cdot \left(\frac{h_b}{h_0}\right)^{0.7}}{1 + 1.5 \cdot \left(\frac{h_b}{h_0}\right)^{0.7}} \tag{15}$$

with the height of the prism h_b = 40 mm and the standard coefficient h_0 = 100 mm according to [24]. Thus $f_{ctm,prism}$ = 3.88 MPa, that does not match with the first crack tensile stress obtained in the series of the uniaxial experiments and equals to $f_{ctm,exp}$ =5.64 MPa. To overcome the presented weak aspect of the material models, it is recommended to use the experimental first crack stress for the material model assembly as $\sigma_{mu} = f_{ctm,exp}$ [20,35].

The selected textile reinforcement behaviour is assumed to be linear [36] for the provided calculations with an elastic modulus E of 251.5 GPa acc. to Table 3. To simplify, the concrete behaviour under pressure is modelled in a bilinear approach, considering a mean compression strength value of $f_{\mathrm{cm}} =$ 114.8 MPa. Furthermore, the material density ρ_c of the concrete taken from the standard prisms with 2,340 kg/m^3 was included in the FEM model.

4. FEM Model Formulation

As mentioned before, the commercial software RFEM [17] was selected for the FE calculations. The software package possesses a set of materials models with different drawbacks and benefits. The TRC material behaviour can be used as an input. In the following, we provide an overview of the three most feasible material models available in the user interface of RFEM which were verified to be used for simulation of TRC structures via the smeared approach.

- For a broad representation of the available material models in the RFEM software package, firstly, a linear elastic material model was considered, called M1 in the further comparisons. This approach can be interesting in order to reflect the material model that is considered as the preinstalled one to be used for calculation of concrete structures in RFEM. The CUBE project shows that such approaches can be properly used [37]. Here, the force flow over the whole structure was first simulated using the linear material model coupled with an appropriate cross-sectional stiffness. Then for an appropriate deflection calculation, the cross-section stiffness was reduced.
- The next material model M2 is based on M1 but it is enriched for tension with plastic zone and consequent strain-hardening zone. Thus, the model is able to reflect either ACK or trilinear material behaviour described above. Within the RFEM user interface it is possible to find an Isotropic Nonlinear Elastic 2D/3D material model which is suitable for calculation of non-linear materials in surfaces. One of the model's features is the possibility to provide a stress-strain curve derived from uniaxial TRC tests. A Mohr-Coulomb yield criterion is used suitable for describing brittle materials such as concrete. The linear envelope based on the yield criteria fits for concrete with a significantly higher compressive than tensile strength. As a result, an asymmetric stress-strain diagram can be used as an input.
- The further development step regarding the material models is M3. It also gives the possibility to model TRC with nonlinear behaviour and named in RFEM environment as Isotropic Damage 2D/3D model. The difference is that the model is based on the assumptions of Mazars' damage model [38,39]. This approach provides an isotropic description of the damaged state of concrete acc. to [39]. The used damage function depends on scalar value D that is split into the two parts D_t for tension and D_c for compression, that can be determined from uniaxial tests. Such special features make the model attractive to be used for calculation of TRC structures after conduction of uniaxial tests. Though, it is important to indicate that the Mazars' model acc. to RFEM description [38] was developed for calculation of materials with strain softening behaviour like plain or steel fiber concrete. Thus, the Mazars' model does not fit to the strain hardening response of TRC via a smeared approach. Nevertheless, in the presented study, The M3 model was used for comparative simulation of TRC.

Figure 8 shows a stress-strain diagram of TRC within RFEM software user interface which was implemented as input data for each of the mentioned above RFEM models. For simplification, the compressive range of the concrete material selected was solved as bilinear curve. The numerical representation of the stress-strain diagrams for ACK and trilinear models for tensile and compressive ranges is given in Table 5.

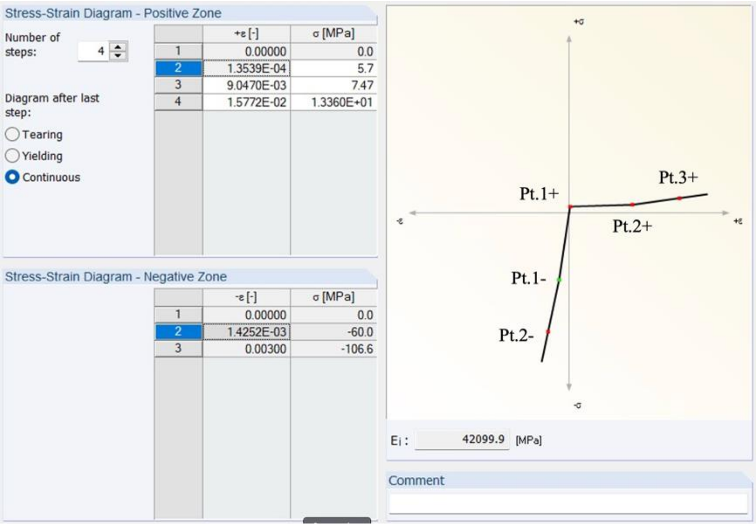

Stress-Strain Diagram - Positive Zone

Number of steps: 4

	+ε [-]	σ [MPa]
1	0.00000	0.0
2	1.3539E-04	5.7
3	9.0470E-03	7.47
4	1.5772E-02	1.3360E+01

Diagram after last step:

○ Tearing
○ Yielding
● Continuous

Stress-Strain Diagram - Negative Zone

	-ε [-]	σ [MPa]
1	0.00000	0.0
2	1.4252E-03	-60.0
3	0.00300	-106.6

Ei : 42099.9 [MPa]

Comment

Figure 8. RFEM user interface with implemented stress-strain diagram. Graphic: Iurii Vakaliuk.

Table 5. Key points of stress-strain diagram for various material models acc. to Figure 8

Diagram points	**Strain (‰)** **ACK ǀ Trilinear**	**Stress (MPa)** **ACK ǀ Trilinear**
Pt. 1 +	0.14 ǀ 0.14	5.70 ǀ 5.70
Pt. 2 +	6.80 ǀ 9.05	5.70 ǀ 7.47
Pt. 3 +	15.90 ǀ 15.77	13.36 ǀ 13.36
Pt. 1 -	0.0	–60.0
Pt. 2 -	–3.0	–106.6

For numerical analysis stability and redundancy in case of peak values of the applied load, the material model was defined with continuous behaviour after reaching the last point in the stress-strain diagram. To estimate the critical load, though, the later (chapter 6) presented calculations were performed stepwise. After each loading step in workflow Step II, the stress conditions were transferred to Step III for postprocessing and verification of the textile failure criteria (compare chapter 5).

In addition, the following RFEM software settings were commonly used for all calculations. The Poisson's ratio μ was set as 0.2 [40]. Furthermore, the TRC shells were modelled within RFEM using 2D quadrangle elements with 4 nodes at corners. Degrees of freedom in nodes are displacement (u_x, u_y, u_z) and rotation $(\varphi_x, \varphi_y, \varphi_z)$ [17]. The selected maximum FEM mesh size was 25 mm. TRC structures to be calculated assumed to be thin-walled with considerably smaller thickness than dimensions in other directions, thus plain-stress conditions were assumed. Within RFEM, shell elements were modelled with constant thickness over the whole element. Thus, stiffness of the elements represented as stiffness of a rectangular cross-section.

To initially validate the introduced above material models within the RFEM user interface, a numerical reconstruction of the uniaxial tensile test was conducted. Figure 9 shows the resulting stress-strain diagram for the three RFEM models M1–M3 with both ACK and trilinear material models. The difference between both is especially noticeable in State of multiple cracking (IIa). Obviously, ACK shows less stiff behaviour. The difference between the approaches used for M2 and M3 is noticeable but not significant.

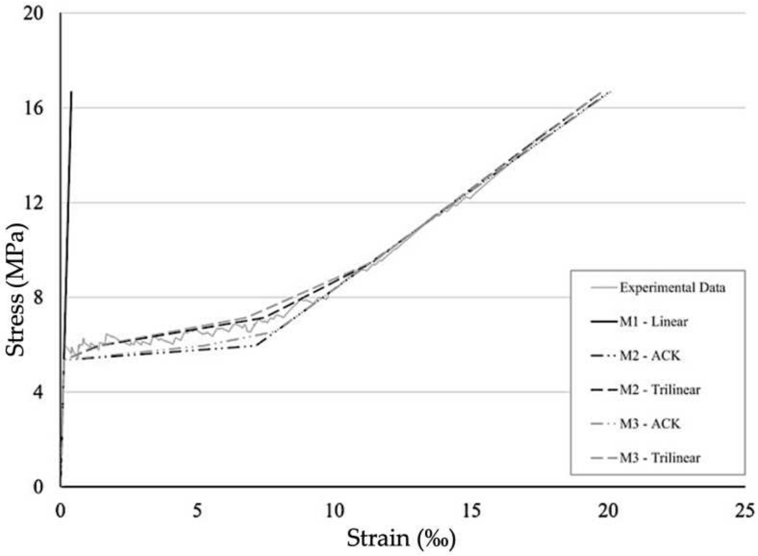

Figure 9. Reconstructed uniaxial tests in RFEM using various material models, Graphic: Iurii Vakaliuk.

5. Textile Failure Criteria Post-Processing

To start with Step III of the workflow, the resulting values have to be exported to stand-alone Python-based scripts. For further processing, a field of strain values $\varepsilon_i^+(\varphi_j)$ and $\varepsilon_i^-(\varphi_j)$ for the positive and negative side of the shell elements respectively should be exported for each FEM node point i for two principal stress axis directions j. Thus, the FEM nodes form a set of vectors $\boldsymbol{x} \in X$ that defines a space X. Figure 10 shows the strain components derived from the FEM calculation.

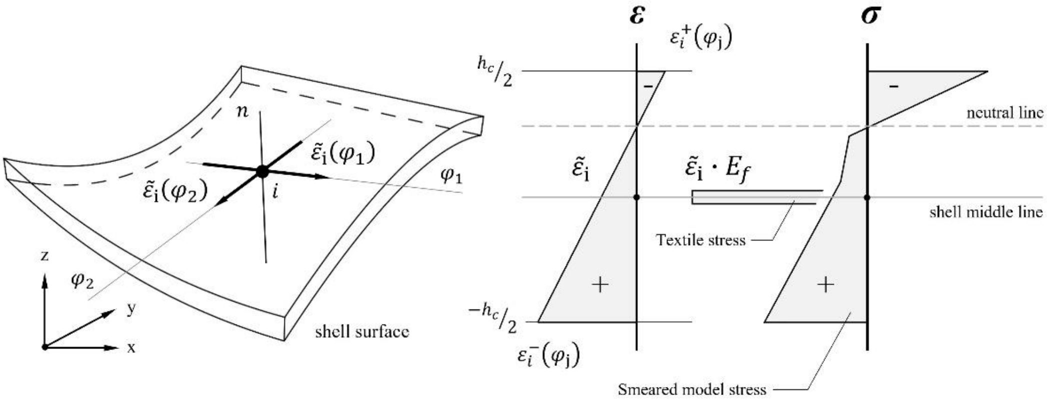

Figure 10. The shell strain and stress state, Graphic: Iurii Vakaliuk.

The selected smeared material model approach possesses a significant limitation: It is impossible to correctly model the position of the reinforcement and as a result, the inner lever arm in case of bending. This may lead to an overestimation of stiffness in case of significant bending [19]. It is assumed that the textile reinforcement is arranged symmetrically in the shell cross-section. Based on the central position of the reinforcement, the strain level $\tilde{\varepsilon}_i$ in each FEM point from X for the textile reinforcement layers and corresponding in-plane tensile forces $n_{Et}(\varphi_j)$ can be estimated as follows:

$$\tilde{\varepsilon}_i = 0.5 \cdot \sum \left(\varepsilon_i^+(\varphi_j),\ \varepsilon_i^-(\varphi_j)\right); \quad n_{Et,i}(\varphi_j) = \tilde{\varepsilon}_i \cdot E_f \cdot A_{tex} \ \text{ for } \tilde{\varepsilon}_i \geq 0 \tag{16}$$

where A_{tex} (mm²/m) cross-section area of the textile reinforcement from Table 3. Such an approach gives insight into the resulting stress filed within the textile reinforcement for further comparative analysis. The resulting concrete in-plane force may be estimated according to Eq. (23):

$$\sigma_{i,Ec}(\varphi_j) = -\int_{-h_c/2}^{+h_c/2} \varepsilon_i(\varphi_j, h)\cdot E_m\,dh;\;\; n_{i,Ec}(\varphi_j) = \sigma_{i,Ec}(\varphi_j)\cdot h_c \;\text{ for }\; \varepsilon_i \le 0 \tag{17}$$

with h_c the height of the TRC shell. After the assessment of the principal stress field, another question arises: how to estimate the limit of the structure properly if axial forces as well as bending moments act simultaneously. A solution is the use of the n-m interaction diagram in a similar way as for steel-reinforced concrete [41]. In recent research on TRC structures, a simplified and normalized η_n-η_m interaction diagram was proposed [41–43]. This can be constructed using experimentally derived strength characteristics for uniaxial tension n_{Rt} (kN/m), uniaxial compression n_{Rc} (kN/m) and pure bending m_R (kNm/m), assuming linear interpolation between them (Figure 11).

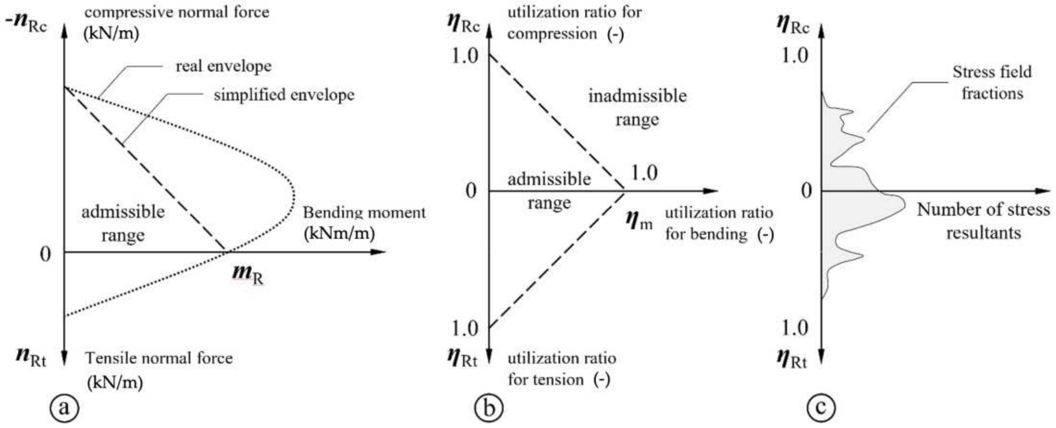

Figure 11. Interaction diagrams proposed for TRC shell structures; (a) n-m initial diagram; (b) η_n-η_m simplified and normalized diagram [41,43]; (c) modified interaction diagram considering the calculation strategy of the project.

The normalized stress resultants can be calculated based on the characteristic strength values:

$$\eta_{nt} = \frac{n_E}{n_{Rt}};\qquad \eta_{nc} = -\frac{n_E}{n_{Rc}};\qquad \eta_m = \frac{|m_E|}{m_R} \tag{18}$$

with $0 \le \eta \le 1{,}0$. In the general case of combined loading, the utilization ratio η_{nm} can be calculated acc. to [41] as

$$\eta_{nm} = max(\eta_{nt}, \eta_{nc}) + \eta_m \tag{19}$$

The simplified envelope diagram shows the following characteristics [41]:

- In the tension-bending range, linear interpolation gives a relatively well representation of real behaviour.
- In the compression-bending range, the ultimate strength is underestimated by the linear interpolation, lying on the safe side.

In the first stages of the project, for simplification reasons, only in-plane actions were considered according to the general aim of the project to proceed with shell-like structures and membrane action. Therefore, the interaction diagram was to be modified to represent only compression and tension ranges. Figure 11c shows the modified version in the current state of the project. It contains so-called stress field fractions (SF). As a result of the estimation of the stress resultants for each FEM point $\boldsymbol{x} \in X$, the points may be sorted according to their level of utilization in the range [0, 1]. The number of points in total for each level of utilization gives the diagram of SF that helps to estimate and further optimize not only the very limited critical FEM points but also points with degree of utilization less than 1.0 and by this it is possible to make the TRC structure fitter according to the principle ‘form follows force’.

In the FEM calculator described in Chapter 4, an isotropic material model was assumed. Though the orthotropic textile reinforcement exhibits an anisotropic behaviour due to the misfit between the direction of the principal stresses and the orientation of the textile yarns [43]. To account for the possible weakening factor the design limit value for the tensile reinforcement $n_{t,Rd}$ can be modified as follows [41]:

$$n_{Rt}(\alpha) = n_{Rt,0°} \cdot cos(\alpha) \cdot k_\alpha + n_{Rt,90°} \cdot sin(\alpha) \cdot (1 - k_\alpha) \tag{20}$$

where $n_{Rt,0°}$ and $n_{Rt,90°}$ is the strength in 0° and 90° direction, respectively. The reduction factor k_α can be calculated according to [41] via:

$$k_\alpha = 1 - \frac{|\alpha|}{90°} \tag{21}$$

Here, α is the deviation angle between the direction of the principal tensile stress and the orientation of the textile yarns. In the TRC shell structure presented in Chapter 6, the warp yarns of the textile grid are aligned in the longitudinal direction of the TRC shell and thus match the assumed principal stress field axis. Thus, $\alpha = 0°$ and consequently $n_{Rt}(\alpha) = n_{Rt,0°}$. The same approach and simplification are valid for the reduction of the tensile strength due to discontinues in the reinforcement layers [41]. It can be encountered via a strength reduction factor that includes the number of textile layers n_f and the number of interruptions $n_{f,int}$ that forms an overlapping of the textile layers in the next expression:

$$k_b = \frac{n_f - n_{f,int}}{n_f} \tag{22}$$

For the narrow width shells, we consider in the project, it is possible to place a complete single layer over the entire structure. The reduction factor thus can be estimated as $k_b = 1$. To summarize, the final expressions for the calculation normalized stress resultants, considering the discussed above range of equations Eqn. (18) – (22) can be expressed as follows:

$$\eta_{nc} = -\frac{n_{Ec}(\varphi_1)}{f_{cm} \cdot h_c} \tag{23}$$

$$\eta_{nt} = \frac{n_{Et}(\varphi_1)}{k_b \cdot cos(\alpha) \cdot f_{tm,tex,Q85} \cdot A_{tex}} \tag{24}$$

Getting back to the workflow, the failure state assessment has to be performed for each FEM node $\boldsymbol{x}$ for either the concrete matrix in the compression range or for the reinforcement in the tensile range. Both aspects can be combined to determine the total utilization ratio acc. to Eq. (25), and to specify the type of failure that characterize the TRC structure [41]:

$$\eta_{nm}^{max}(\boldsymbol{x}) = max_{j=1..n}\left[\eta_{nm,j}\left(\alpha_j(\boldsymbol{x}), \boldsymbol{x}\right)\right] \tag{25}$$

The provided above expression has to be verified for all load cases j.

6. Trial-Based Calculation

To validate the provided above material models and selected FEM procedures and to create a basis for the further development of the workflow, an arch-like shell was selected to perform a bending test according to the reference project [44], Figure 12. The total length of the shell is 2,700 mm and the width 600 mm. The transversal profile follows a chain line with the rise of the shell in the middle point of 100 mm. Due to manufacturing aspects, the thickness of the shell was set to be 40 mm. Prior to the experiments, the TRC shell was simulated, in a first step only with one single main layer of the solidian GRID Q85-CCE-21-E5 completely over the whole element. The loading was selected according to EN 1991-1-1 [45] for residential use, comprising a 2.0 kN/m^2 area load and a 3.0 kN point load. In the ultimate limit state, the textile stresses in the tension zone were higher than the design value for the textile. Therefore, it was decided to place two 200 mm wide additional textile stripes symmetrical in the tensile zone of the shell (Figure 12). The textile layers were arranged analogously to the uniaxial tensile samples with 10 mm spacing between the layers and 15 mm concrete cover.

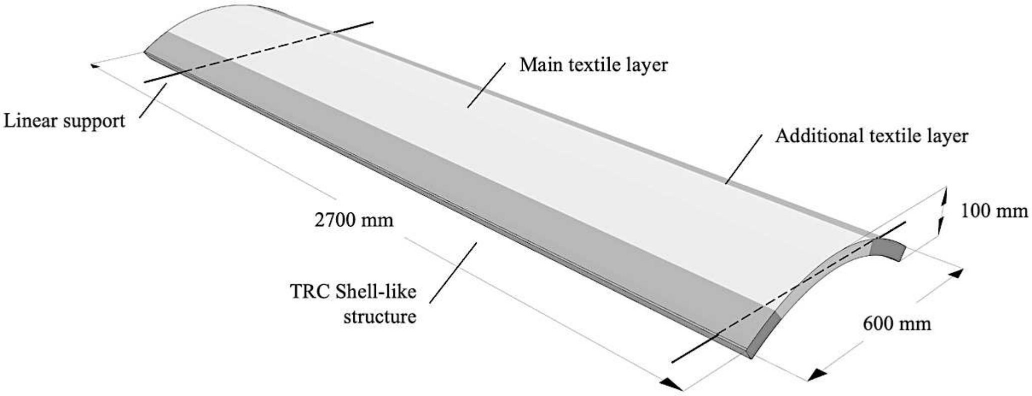

Figure 12. General view of the TRC shell for the trial-based calculation, Graphic: Iurii Vakaliuk.

For validation of the numerical model, laboratory experiments with simulated TRC shells were performed. According to the technical aspects in the lab, the initial area load was converted into four equal line loads, see Figure 13a, resulting in a 6-point bending test. The load was introduced displacement controlled with a velocity of 0.05 mm/s until failure. In total two shells were tested. Figure 13 gives results for the limit stress state that corresponds to 12.1 kN/m for each line load or a total of 31 kN of an accumulated load.

Figure 13a,b show the stress state of the composite, where σ_i^+ stands for the top and σ_i^- for the bottom side of the shell, respectively. As may be seen from the legends, the compression zone lies between the top and bottom sides of the shell. Consequently, the TRC shell possess significant bending action that is in contradiction with the accepted calculation hypothesis. The maximum stress of the concrete matrix reaches the magnitude of –32.7 MPa. That corresponds to only 28.5 % of the experimentally determined concrete strength of f_{cm} = 114.8 MPa. Thus, it is expected to obtain a reinforcement failure during the experiment. Additionally, it indicates that there is still a relatively large space for material optimization that potentially may reduce the compression zone and increase the utilization ratio of the concrete under compression. The reinforcement diagram in Figure 13c shows, that in the middle section of the shell the magnitude of $\tilde{\varepsilon}_i > 0$ and consequently the reinforcement is considered to be activated. In the critical tensile zone of the shell, two layers of reinforcement reach the limit of $f_{tm,tex,Q85}$ = 3,750.0 MPa. The textile tensile strength magnitude was directly calculated from the mean value of composite strength out of the conducted uniaxial tensile experiments (Figures 6 and 7). It can be calculated with modified Eq. (7) as follows:

$$f_{tm,tex,Q85} = \frac{\tilde{\sigma}_{cu}}{V_f} \tag{26}$$

where V_f = 0.4 %; $\tilde{\sigma}_{cu}$ = 15 MPa (ultimate composite's strength). In the bending tests, we detected midpoint deflections between 121.9 and 128.6 mm and reached failure loads between 33.0 and 35.7 kN, resulting in averages of 125.3 mm and 34.4 kN. The failure load acc. to the textile failure estimation procedure described above derived at level of 27.8 kN and 29.7 kN for the material models M2 and M3 respectively.

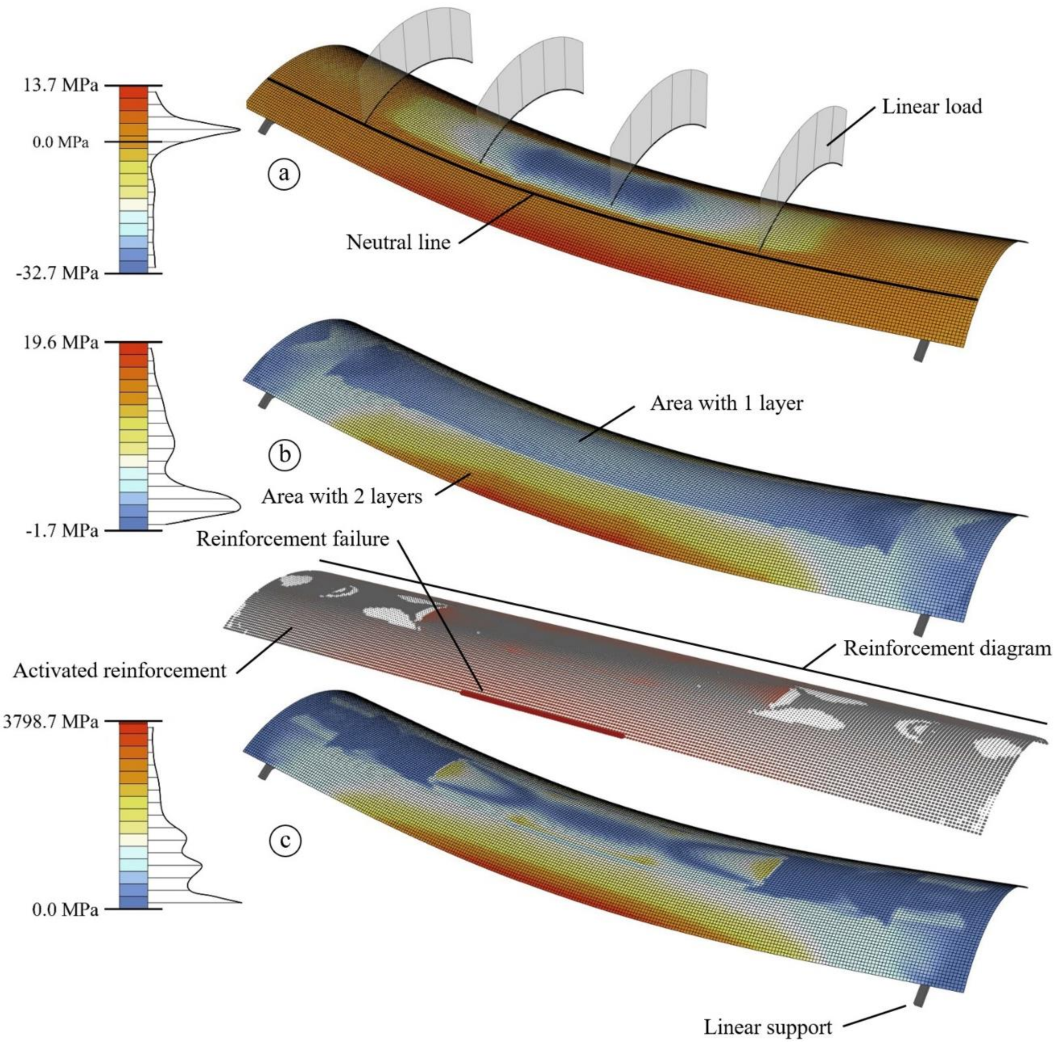

Figure 13. Composite stress state field of the shell according to an accumulated load of 31.0 kN; (a) shell's top side σ_i^+; (b) bottom side of the shell σ_i^-; (c) textile reinforcement stress field, Graphic: Iurii Vakaliuk.

Figure 14 reflects the midspan deflections derived from tested shells and deflection results obtained from numerical analysis using first linear model M1 as a reference and the two different models described above M2 and M3 with variations input data from trilinear and ACK material models.

As expected, the linear model M1 gives good agreement only in the uncracked state. In general, all models show deficits in *State II*. Furthermore, there is a clear influence of the input data developed acc. to trilinear and ACK material model. ACK approach (M2) gives slightly less stiffness behaviour than M3 material model, which matches the experimental data at the end of test a bit better. In general, the overestimation of the stiffness may be a cumulative result of various reasons. Nevertheless, one of the keys envisioned is the smeared model does not give a correct bending load response at the first stages of loading history due to weak behaviour for non-membrane actions regardless of the utilized material model.

Preprints (www.preprints.org) | NOT PEER-REVIEWED | Posted: 11 December 2023 doi:10.20944/preprints202312.0705.v1

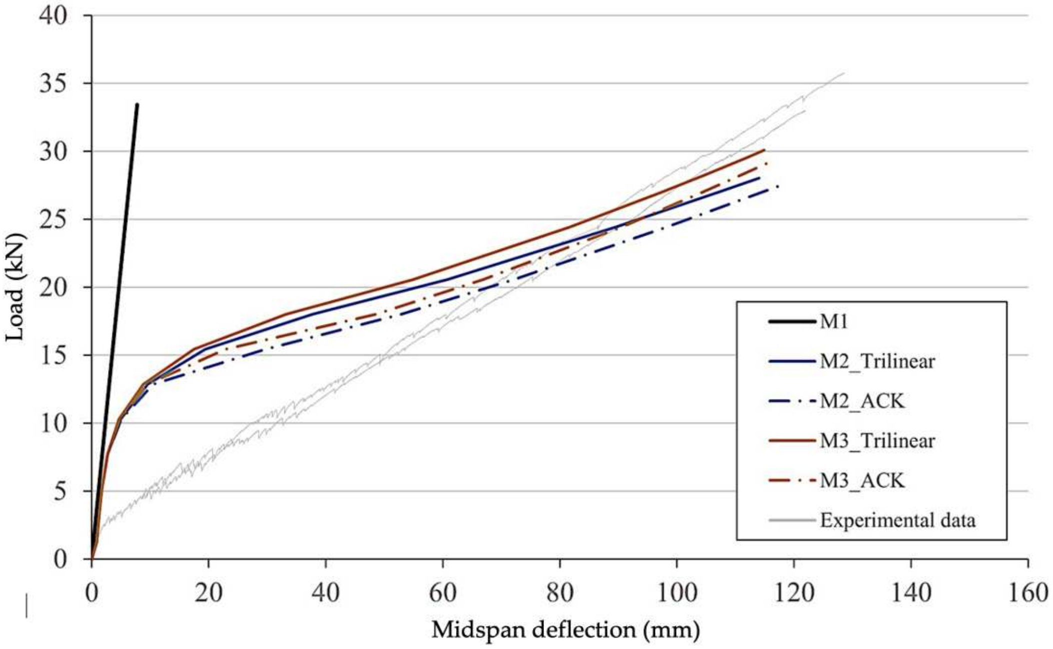

Figure 14. Midspan deflection-force relations determined in the lab tests and in simulations by using M1–M3 material models, Graphic: Iurii Vakaliuk.

The discussion and consequent hypothesis regarding a possible reason for overestimation of the structural stiffness for the tested shell-like structures need to be strengthened. For this purpose, experiments carried out earlier at our institute in another project were used as alternative shell structure (Figure 15); more details are described in [19,44].

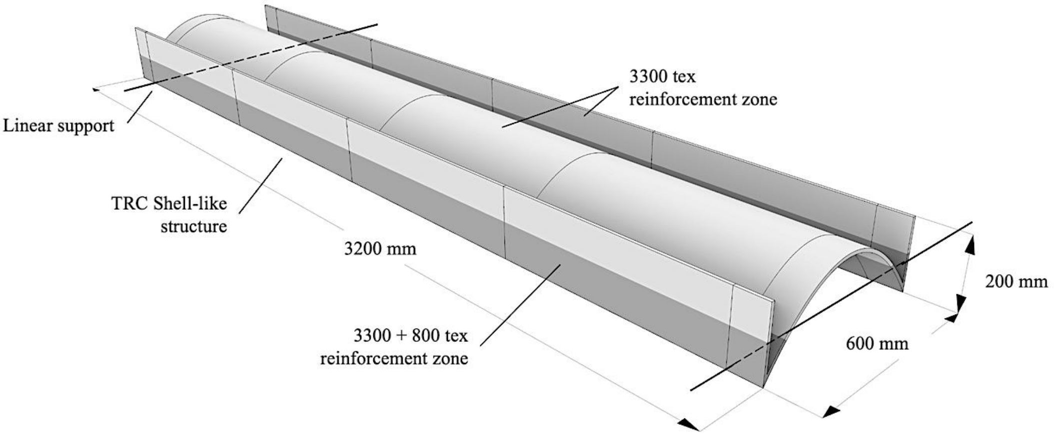

Figure 15. Alternative TRC shell structure, Graphic: Iurii Vakaliuk based on [19,45].

The main shell thickness was 1 cm with minor differences in the middle area of the shell element. The neutral line was located approx. 50 mm from the shell's vertex [44]. Therefore, it may be indicated that top and bottom parts of the shell possess mainly membrane forces in contrast to the previously presented shells with neutral line inside the element's thickness. For comparison purposes, the alternative shell was modelled in RFEM software using the M2 and M3 material models. The stress-strain relations for the models are based on uniaxial tests on the used textiles [19] acc. to ACK methodology. The key points of the stress-strain diagrams are provided in Table 6.

Table 6. Key points of stress-strain diagram in RFEM software for positive range of the material behaviour

Diagram points	Strain (‰)	Stress (MPa)
	3300 tex ǀ 3300+800 tex	3300 tex ǀ 3300+800 tex
Pt. 1 +	0.086 ǀ 0.086	2.40 ǀ 2.40
Pt. 2 +	2.00 ǀ 1.40	2.40 ǀ 2.40
Pt. 3 +	7.20 ǀ 7.30	19.00 ǀ 30.00

In Figure 16, in addition to test values, force-midspan deflection curves from calculations using M2 and M3 models from RFEM are shown as well as a curve derived with smeared approach using ABAQUS software package [19]. It can be seen from the figure, the models M2 and M3 give good agreement with the reference smeared approach calculation and the experimental results. This agreement supports the hypothesis that the smeared TRC calculation approach can be used in RFEM for structures with predominantly membrane actions. It is also important to note that model M3 with Mazars' hypothesis provides also good agreement even though the TRC material behaves in a strain-hardening manner.

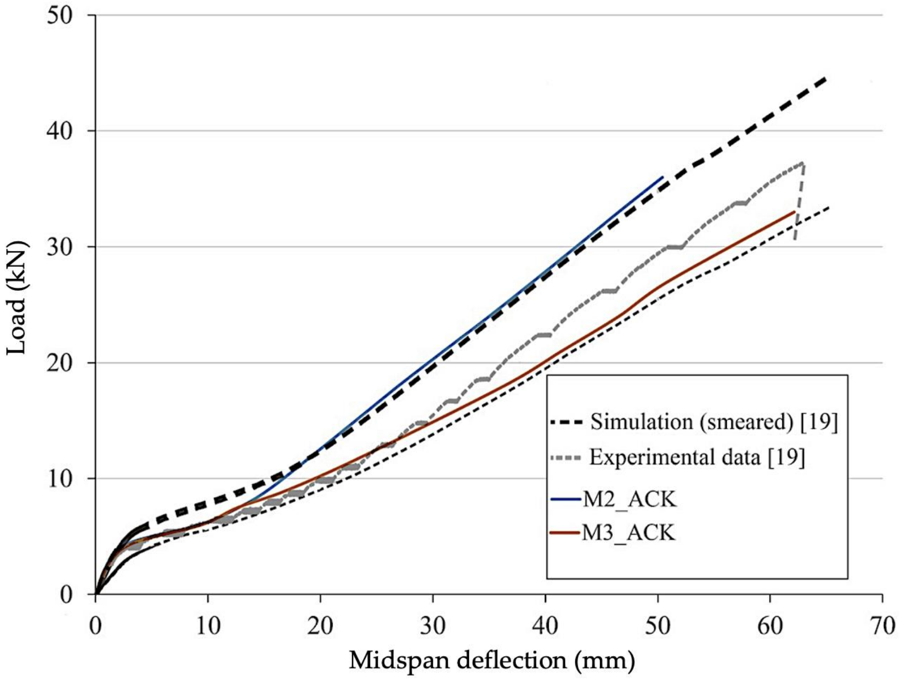

Figure 16. Experimental and calculated force-midspan deflection curves for the alternative TRC shell from [19], Graphic: Ehsan Sharei and Iurii Vakaliuk.

7. Conclusions

First, for the project, the numerical analysis workflow was assembled, and it shows a reasonable response. There is still a list of components to be upgraded like in general the numerical analysis type and failure criteria assessment routines. But the basic components show a good background for further development of analysis routines and enable us to switch now to multiobjective optimization of TRC shell structures. Second, we could show that RFEM software package as a FEM solver can be used for calculation of thin-walled TRC structures acc. to smeared approach, with preinstalled material models and proper calibration based on uniaxial tests. Though the influence of bending action potential may lead to a significant overestimation of the structural stiffness of the TRC structures. Derived results of a comparable research legitimate the further possible step within the scope of the project such as conversion the numerical model to the resolved layer approach mentioned before in the paper. In that way, the TRC structures can be presented as multilayer systems with one layer representing concrete matrix in the shell and the other representing the textile. It will provide more appropriate data for the M3 Mazars' damage model calibrated for brittle-like materials.

A comprehensive numerical parameter study is currently being carried out in the project. The aim is to find out under which conditions, and to which extend a shell load-bearing effect can occur inside a component and what influence, for example, geometrical topology and boundary conditions, imperfections and material properties have. Selected laboratory tests will serve to verify the model.

Author Contributions: Conceptualization, M.C., S.S. and I.V.; methodology, I.V.; validation, I.V. and S.S.; formal analysis, I.V.; investigation, I.V.; writing—original draft preparation, I.V. and S.S.; writing—review and editing, S.S. and I.V.; visualization, I.V. and S.S.; supervision, M.C. and S.S.; project administration, I.V.; funding acquisition, M.C. and S.S. All authors have read and agreed to the published version of the manuscript.

Funding: The authors greatly acknowledge the funding by the Deutsche Forschungsgemeinschaft (DFG, German Research Foundation) in the framework of the Collaborative Research Centre CRC/TRR 280 "Design Strategies for Material-Minimized Carbon Reinforced Concrete Structures – Principles of a New Approach to Construction" (project ID 417002380). The Article Processing Charges (APC) were funded by the joint publication funds of TU Dresden, including Carl Gustav Carus Faculty of Medicine, and the SLUB Dresden as well as the Open Access Publication Funding of the DFG.

Data Availability Statement: The data presented in this study are available on request from the corresponding author. The data are not publicly available due to ongoing study.

Acknowledgments: The authors greatly acknowledge the funding by the Deutsche Forschungsgemeinschaft (DFG, German Research Foundation) in the framework of the Collaborative Research Centre CRC/TRR 280 "Design Strategies for Material-Minimized Carbon Reinforced Concrete Structures – Principles of a New Approach to Construction" (project ID 417002380). For the purpose of comparison, results from the project "Product and process development of light bearing ceiling elements of textile rein-forced concrete for the building in existing" funded by the German Federal Ministry of Economic Affairs and Energy (BMWi, Grant No. KF2505611KI3) were used.

Conflicts of Interest: The authors declare no conflict of interest.

References

1. Bologna, A.; Gargiani, R. *The Rhetoric of Pier Luigi Nervi: Forms in Reinforced Concrete and Ferrocement*. EPFL Presses Polytechniques et Universitaires Romandes, 2016.
2. Mata-Falcon, J.; Bischof, P.; Huber, T.; Anton, A.; Burger, J.; Ranaudo, F.; Jipa, A.; Gebhard, L.; Reiter, L.; Lloret-Fritschi, E.; et al. Digitally Fabricated Ribbed Concrete Floor Slabs: A Sustainable Solution for Construction. *RILEM Technical Letters* **2022**, *7*, 68–78, doi:10.21809/rilemtechlett.2022.161.
3. Frenzel, M.; Farwig, K.; Curbach, M. Leichte Deckentragwerke aus geschichteten Hochleistungsbetonen | Lightweight Ceiling Structures Made of Layered High-Performance Concrete. In *SPP 1542: Leicht Bauen mit Beton. Grundlagen für das Bauen der Zukunft mit bionischen und mathematischen Entwurfsprinzipien (Abschlussbericht) | SPP 1542: Concrete Light. Future Concrete Structures using Bionic, Mathematical and Engineering Formfinding Principles (Final Report)*; Scheerer, S.; Curbach, M., Eds., Dresden: Institut für Massivbau der TU Dresden, 2022, 144–169, doi:10.25368/2022.162.
4. Cuypers, H.; Wastiels, J. Analysis and Verification of the Performance of Sandwich Panels with Textile Reinforced Concrete Faces. *Journal of Sandwich Structures & Materials* **2011**, *13*, 589–603, doi:10.1177/1099636211408665.
5. Frenzel, M. *Zum Tragverhalten von Leichten, Geschichteten Betondecken* [dissertation]. Technischen Universität Dresden, Dresden, Germany, 2021, URL: https://nbn-resolving.org/urn:nbn:de:bsz:14-qucosa2-787009.
6. Williams Portal, N.; Flansbjer, M.; Zandi, K.; Wlasak, L.; Malaga, K. Bending Behaviour of Novel Textile Reinforced Concrete-foamed Concrete (TRC-FC) Sandwich Elements. *Composite Structures* **2017**, *177*, 104–118, doi: 10.1016/j.compstruct.2017.06.051.
7. Schmeer, D.; Sobek, W. Gradientenbeton. In *Beton-Kalender 2019*; Bergmeister, K.; Fingerloos, F.; Wörner, J.-D., Eds., Berlin: Ernst & Sohn, 2019, 455–476, doi: 10.1002/9783433609330.ch6.

8. Schmeer, D.; Wörner, M.; Garrecht, K.; Sawodny, O.; Sobek, W. Effiziente Automatisierte Herstellung Multifunktional Gradierter Bauteile Mit Mineralischen Hohlkörpern | Efficient Automated Production of Multifunctional Graded Components with Mineral Hollow Bodies. In *SPP 1542: Leicht Bauen mit Beton. Grundlagen für das Bauen der Zukunft mit bionischen und mathematischen Entwurfsprinzipien (Abschlussbericht) | SPP 1542: Concrete Light. Future Concrete Structures using Bionic, Mathematical and Engineering Formfinding Principles (Final Report)*; Scheerer, S.; Curbach, M., Eds., Dresden: Institut für Massivbau der TU Dresden, 2022, 250–282, doi:10.25368/2022.331.
9. Beckmann, B.; Bielak, J.; Bosbach, S.; Scheerer, S.; Schmidt, C.; Hegger, J.; Curbach, M. Collaborative Research on Carbon Reinforced Concrete Structures in the CRC/TRR 280 Project. *Civil engineering design* **2021**, *3*, 99–109, doi:10.1002/cend.202100017.
10. Main website of Collaborative Research Centre/Transregio 280, (CRC/TRR 280), available online: https://www.sfbtrr280.de/en/. [accessed on 09.12.2023]
11. Hegger, J.; Curbach, M.; Stark, A.; Wilhelm, S.; Farwig, K. Innovative Design Concepts: Application of Textile Reinforced Concrete to Shell Structures. *Structural Concrete* **2018**, *19*, 637–646, doi:10.1002/suco.201700157.
12. McNeel Europe SL, Rhinoceros 3D, Version 7.0 Available online: https://www.rhino3d.com/. [accessed on 09.12.2023]
13. Robert McNeel & Associates, Grasshopper 3D, Version 7.0 Available online: https://www.grasshopper3d.com/. [accessed on 09.12.2023]
14. RF-COM/RS-COM Add-on Module for RFEM/RSTAB Available online: https://www.dlubal.com/en/products/rfem-and-rstab-add-on-modules/others/rf-com. [accessed on 09.12.2023]
15. Vakaliuk, I.; Frenzel, M.; Curbach, M. Application of Parametric Design Tools for the Roof of the C³ Technology Demonstration House – CUBE. In *Form and Force – Proc. of the IASS Annual Symp. 2019/Structural Membranes 2019*; Barcelona, Spain; Lázaro, C.; Bletzinger, K.-U.; Oñate, E., Eds., 2019, 1077–1084.
16. Koschemann, M.; Vakaliuk, I.; Curbach, M. An Ultra-Light Carbon Concrete Bridge: From Design to Realisation. In *Concrete Innovation for Sustainability – Proc. for the 6th fib International Congress 2022*, 12.–16.06.2022 in Oslo (Norway); Stokkeland, S.; Braarud, H. C., Eds., Oslo: Novus Press, 2022, 2458-2467.
17. Dlubal Software GmbH, RFEM, Version 5.19, available online: www.dlubal.com. [accessed on 09.12.2023]
18. Vakaliuk, I.; Platen, J.; Klempt, V.; Scheerer, S.; Curbach, M.; Kaliske, M.; Löhnert, S. Development of Load-Bearing Shell-Type TRC Structures – Initial Numerical Analysis. In *Concrete Innovation for Sustainability – Proc. for the 6th fib International Congress 2022*, 12.–16.06.2022 in Oslo (Norway); Stokkeland, S.; Braarud, H. C., Eds., Oslo: Novus Press, 2022, 1235–1244.
19. Chudoba, R.; Sharei, E.; Senckiel-Peters, T.; Schladitz, F. Numerical Modelling of Non-Uniformly Reinforced Carbon Concrete Lightweight Ceiling Elements. *Applied Sciences* **2019**, *9*, doi:10.3390/app9112348.
20. Jesse, F. *Tragverhalten von Filamentgarnen in zementgebundener Matrix* [dissertation]. Technische Universität Dresden, Dresden, Germany, 2005, URL: https://nbn-resolving.org/urn:nbn:de:swb:14-1122970324369-39398.
21. Hartig, J. *Numerical Investigations on the Uniaxial Tensile Behaviour of Textile Reinforced Concrete* [dissertation]. Technischen Universität Dresden, Institut für Massivbau, Dresden, Germany, 2011.
22. Bentur, A.; Mindess, S. *Fibre Reinforced Cementitious Composites*. Modern Concrete Technology Series; E & FN Spon; ISBN10: 0–415–25048–X (hbk).
23. Nathan, G.K.; Paramasivam, P.; Lee, S.L. Tensile Behaviour of Fiber Reinforced Cement Paste. *Journal of Ferrocement* **1977**, *7*, 59–79.
24. CEB-FIP Model Code 1990: Design Code. London: T. Telford, 1993.
25. Blom, J.; Wastiels, J. Modelling Textile Reinforced Cementitious Composites – Effect of Elevated Temperatures. In *Proceedings of the 19th Int. Conf. on Composite Materials*, 2013, 7098–7108.
26. Blom, J.; Cuypers, H.; Van Itterbeeck, P.; Wastiels, J. Modelling the Behaviour of Textile Reinforced Cementitious Composites under Bending. In *Proc. Fibre Concrete 2007 Technology, Design, Application*, 12–13 September 2007 in Prague; Kohoutková, A., Ed., 2007, 205–210.

27. Jesse, F.; Ortlepp, R.; Curbach, M. Tensile Stress-Strain Behaviour of Textile Reinforced Concrete. In *Towards a better built environment – inovation, sustainability, information technology – Proc. of the IABSE Symp. 2002*, Melbourne, September 2002, publ. in IABSE Symposium Report 86(7), 2002. 376–377.
28. Zilch, K.; Zehetmaier, G. *Bemessung im konstruktiven Betonbau: Nach DIN 1045-1 Und EN 1992-1-1*. 2nd ed.; Berlin Heidelberg: Springer-Verlag, 2010; ISBN 978-3-540-70637-3.
29. Ng, H.K.; Nathan, G.K.; Paramasivam, P.; Lee, S.L. Tensile Properties of Steel Fiber Reinforced Mortar. *Journal of Ferrocement* **1978**, *8*, 219–229.
30. Carbon Concrete Composite [homepage], available online: https://www.bauen-neu-denken.de/en/. [accessed on 09.12.2023]
31. Wilhelm, K. Verbundverhalten von mineralisch und polymer gebundenen Carbonbewehrungen und Beton bei Raumtemperatur und erhöhten Temperaturen bis 500 °C [dissertation]. Technische Universität Dresden, Germany, 2021, https://nbn-resolving.org/urn:nbn:de:bsz:14-qucosa2-770999.
32. DIN EN 196-1:2016-11: Prüfverfahren für Zement – Teil 1: Bestimmung der Festigkeit. Berlin: Beuth Verlag, 2016.
33. Technical Data Sheet Solidian GRID Q85-CCE-21-E5. 2023.
34. Vakaliuk, I.; Scheerer, S.; Curbach, M. Initial Laboratory Test of Load-Bearing Shell-Shaped TRC Structures. In *Concrete Innovation for Sustainability – Proc. for the 6th fib International Congress 2022*, 12.–16.06.2022 in Oslo (Norway); Stokkeland, S.; Braarud, H. C., Eds., Oslo: Novus Press, 2022, 675–684.
35. Schütze, E.; Bielak, J.; Scheerer, S.; Hegger, J.; Curbach, M. Einaxialer Zugversuch für Carbonbeton mit textiler Bewehrung | Uniaxial Tensile Test for Carbon Reinforced Concrete with Textile Reinforcement. *Beton- und Stahlbetonbau* **2018**, *113*, 33–47, doi:10.1002/best.201700074.
36. Rempel, S. Zur Zuverlässigkeit der Bemessung von biegebeanspruchten Betonbauteilen mit textiler Bewehrung [dissertation]. RWTH Aachen, Aachen, Germany, 2018, doi:10.18154/RWTH-2019-01098.
37. Zavadski, V.; Frenzel, M. Aufbau, Bemessung und Planung der TWIST-Carbonbetonschalen. *Beton- und Stahlbetonbau* **2023**, *118, S2*, 71–81, doi:10.1002/best.202300009.
38. Mazars, J.; Grange, S. Simplified Strategies Based on Damage Mechanics for Concrete under Dynamic Loading. *Phil. Trans. R. Soc. A* **2017**, *375, 20160170,* doi:10.1098/rsta.2016.0170.
39. Mazars, J. A Description of Micro- and Macroscale Damage of Concrete Structures. *Engineering Fracture Mechanics* **1986**, *25*, 729–737.
40. Sharei, E. Simulation Concepts for Concrete Structures with Discrete and Smeared Representation of Reinforcement [dissertation]. RWTH Aachen, Aachen, Germany, 2018.
41. Scholzen, A.; Chudoba, R.; Hegger, J. Thin-Walled Shell Structures Made of Textile-Reinforced Concrete. *Structural Concrete* **2015**, *16*, 115–124, doi:10.1002/suco.201400046.
42. Sharei, E.; Chudoba, R.; Scholzen, A. Cross-Sectional Failure Criterion Combined with Strain-Hardening Damage Model for Simulation of Thin-Walled Textile-Reinforced Concrete Shells. In *Proc of the In ECCOMAS Congress 2016 VII European Congress on Computational Methods in Applied Sciences and Engineering;* M. Papadrakakis, V. Papadopoulos, G. Stefanou, V. Plevris, Eds., Crete Island, Greece, 2016, 6823–6831.
43. Scholzen, A.; Chudoba, R.; Hegger, J. Ultimate Limit State Assessment of TRC Shell Structures with Combined Normal and Bending Loading. In *Proc. of 11th Int. Symp. on Ferrocement and Textile Reinforced Concrete*, Aachen, June 2015, publ. in RILEM Publ. Proc., Bagneux: RILEM Publ., 2015, 159–166.
44. Senckpiel, T.; Haussler-Combe, U. Experimental and Computational Investigations on Shell Structures Made of Carbon Reinforced Concrete. In *Interfaces: Architecture, Engineering, Science – Proc. of Annual Meeting of the International Association of Shell & Spatial Structures (IASS)*, Hamburg, 25-27 September 2017, 2017, 1–8(8).
45. EN 1991-1-1, Eurocode 1: Actions on Structures - Part 1-1: General Actions – Densities, Self-Weight, Imposed Loads for Buildings.